ACCOUNTS
of chemical research

Coherent Multidimensional Optical Probes for Electron Correlations and Exciton Dynamics: From NMR to X-rays

SHAUL MUKAMEL,* DARIUS ABRAMAVICIUS, LIJUN YANG, WEI ZHUANG,‡ IGOR V. SCHWEIGERT,¶ AND DMITRI V. VORONINE§

Department of Chemistry, University of California, Irvine, California

RECEIVED ON NOVEMBER 24, 2008

CONSPECTUS

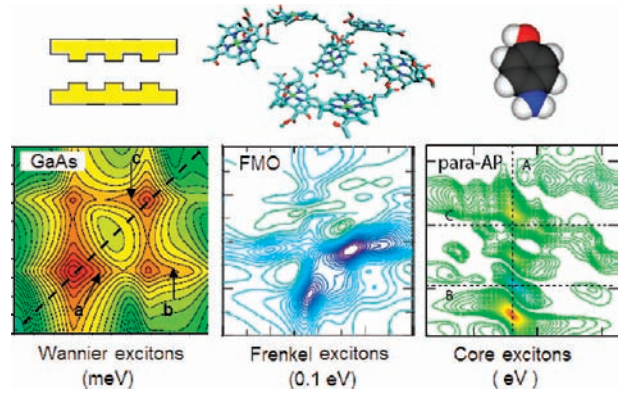

Over the past 15 years, researchers have extended the multidimensional techniques which originated with NMR in the 1970s to infrared and visible coherent spectroscopy. These advances have dramatically enhanced the temporal resolution from the microsecond to the femtosecond regime.

NMR spectroscopists have developed principles for the design of pulse sequences that enhance selected spectral features and reveal desired dynamical events. Extending these principles to the optical regime offers numerous opportunities for narrowing the line shapes in specific directions, unraveling weak cross-peaks from otherwise congested spectra, and controlling the interferences between quantum pathways. We can achieve these enhancements by shaping the spectral and temporal profiles of the pulses. Pulse polarization shaping may lead to unique probes of time-dependent chirality.

In this Account, we compare two types of signals. The first, the photon echo, is generated in the direction $-\mathbf{k}_1 + \mathbf{k}_2 + \mathbf{k}_3$, and the second, double quantum coherence, is detected at $+\mathbf{k}_1 + \mathbf{k}_2 - \mathbf{k}_3$. Here $\mathbf{k}_1$, $\mathbf{k}_2$, and $\mathbf{k}_3$ are the wave vectors of the three incoming pulses in chronological order. We illustrate the novel information extracted from these signals by simulations of three physical systems. In the first system, spectra of GaAs semiconductor quantum wells provide a direct look at many-body electron correlation effects. We directly observe specific projections of the many-electron wave function, which we can use to test the quality of various levels of computational techniques for electronic structure. Secondly, the spectra of photosynthetic aggregates reveal couplings between chromophores, quantum coherence signatures of chromophore entanglement, and energy-transfer pathways. Using some fundamental symmetries of pulse polarization configurations of nonlinear signals, we can construct superpositions of signals designed to better distinguish among various coherent and incoherent exciton transport pathways and amplify subtle variations among different species of the Fenna–Matthews–Olson (FMO) antenna complex. Both of the first two applications require femtosecond pulses of light in the visible range. The third application demonstrates how resonant core spectroscopy may be used to generate core excitations that are highly localized at selected atoms. Such signals can monitor the motions of valence electron wavepackets in real space with atomic spatial resolution.

These future X-ray applications will require attosecond bright X-ray sources, which are currently being developed in several labs. Common principles underlie these techniques in coherent spectroscopy for spins, valence electrons, and core electronic excitations, spanning frequencies from radiowaves to hard X-rays.

Published on the Web 03/26/2009 www.pubs.acs.org
10.1021/ar800258z CCC: $71.50

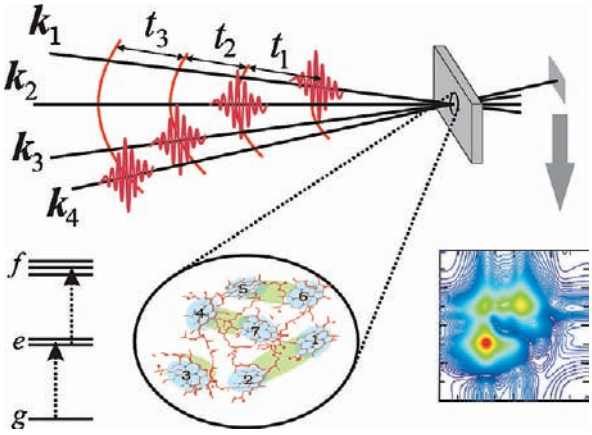

FIGURE 1. Scheme of the time-resolved four-wave-mixing experiment. All calculations are given for the three-band model system shown on the bottom left.

Introduction

Linear spectroscopy is *one-dimensional* (1D); the absorption spectrum provides information about excitation energies and transition dipoles as projected into a single frequency axis. In contrast, *multidimensional* optical spectroscopy uses sequences of laser pulses to perturb or label the electronic degrees of freedom and watch for correlated events taking place during several controlled time intervals. The resulting correlation plots can be interpreted in terms of multipoint correlation functions that carry considerably more detailed information on dynamical events than the two-point functions provided by 1D techniques.[1−7] Correlations between spins have been routinely used in NMR to study complex molecules. The Nobel prize was awarded to Richard Ernst[8] for inventing the technique and to Kurt Wüthrich[9] for developing pulse sequences suitable for large proteins. Optical analogues of 2D NMR techniques first designed to study vibrational dynamics by Raman or infrared pulses[1] and later extended to resonant electronic excitations in chromophore aggregates[10] have been made possible thanks to the development of stable femtosecond laser sources with controlled phases.[11] In an ideal heterodyne-detected 2D experiment (Figure 1), three laser pulses with wavevectors $\mathbf{k}_1$, $\mathbf{k}_2$, and $\mathbf{k}_3$ interact sequentially with the molecules in the sample to create a polarization with wavevector $\mathbf{k}_4$ given by one of the linear combinations $\pm\mathbf{k}_1 \pm \mathbf{k}_2 \pm \mathbf{k}_3$. In all other directions the polarization vanishes due to the random phases of contributions from different molecules. The coherent signal is generated in directions close to the various possible $\mathbf{k}_4$. The mismatch caused by frequency variation of the index of refraction is optimized ("phase matched") to generate an intense signal detected by interference with a fourth pulse at the desired wavevector $\mathbf{k}_4$. When the radiation field is described quantum mechanically the entire process can be viewed as a concerted four photon process. The signal $S(t_3, t_2, t_1)$ depends parametrically on the time intervals between pulses, which constitute the primary control parameters. Other parameters include the direction $\mathbf{k}_4$, pulse polarizations, envelope shapes, and even the phases.

We shall illustrate the power of 2D techniques and how they work using the three-band model system shown in Figure 1, which has a ground state (*g*), a singly excited manifold (*e*) and a doubly excited manifold (*f*). The dipole operator can induce transitions between *g* and *e*, and *e* to *f*. All transitions in the system are stimulated: spontaneous emission is neglected. This three-band model represents electronic excitations in the various physical systems covered in this Account.

Multidimensional signals monitor the dynamics of the system's density matrix during the time intervals between pulses. Diagonal elements of this matrix, ρ_{nn}, represent *populations* of various states, while the off diagonal elements, ρ_{nm} ($n \neq m$), known as *coherences*, carry additional valuable phase information. These signals can be described intuitively using the Feynman diagrams shown in Figure 2, which display the *Liouville space pathways*: sequences of interactions with the various fields and the relevant elements of the density matrix during the controlled intervals between interactions.[6,29] The left and right vertical lines represent the ket and the bra of the density matrix, respectively. Time runs from bottom to top, and the labels mark the density matrix elements during the evolution periods between interactions. The arrows represent interactions with photons and are labeled by their wavevectors. Photon absorption is accompanied by a molecular excitation (*g* to *e* or *e* to *f* transition), whereas photon emission induces deexcitation (*e* to *g* or *f* to *e*).

Our discussion will focus on two signals: the photon-echo $S_{\mathbf{k}_\mathrm{I}}$ with $\mathbf{k}_\mathrm{I} = -\mathbf{k}_1 + \mathbf{k}_2 + \mathbf{k}_3$ and the double-quantum-coherence $S_{\mathbf{k}_\mathrm{III}}$ with $\mathbf{k}_\mathrm{III} = +\mathbf{k}_1 + \mathbf{k}_2 - \mathbf{k}_3$. We first present the Feynman diagrams and the quantum pathways relevant for the two techniques for the generic exciton model of Figure 1. Simulated signals are then presented for three physical systems: Wannier excitons in semiconductor quantum wells,[12−15] Frenkel excitons in photosynthetic complexes,[6,7] and soft X-ray core excitons in molecules.[16−19] We demonstrate that both techniques provide new insights into the structure and exciton dynamics in semiconductor nanostructures and molecular aggregates and are highly sensitive to the separation between core−shells and the localization of the core-excited states.

The three contributions to the $S_{\mathbf{k}_\mathrm{I}}$ signal depicted in Figure 2 are known as ground-state bleaching (GSB), excited-state stimulated emission (ESE), and excited-state absorption (ESA).[6]

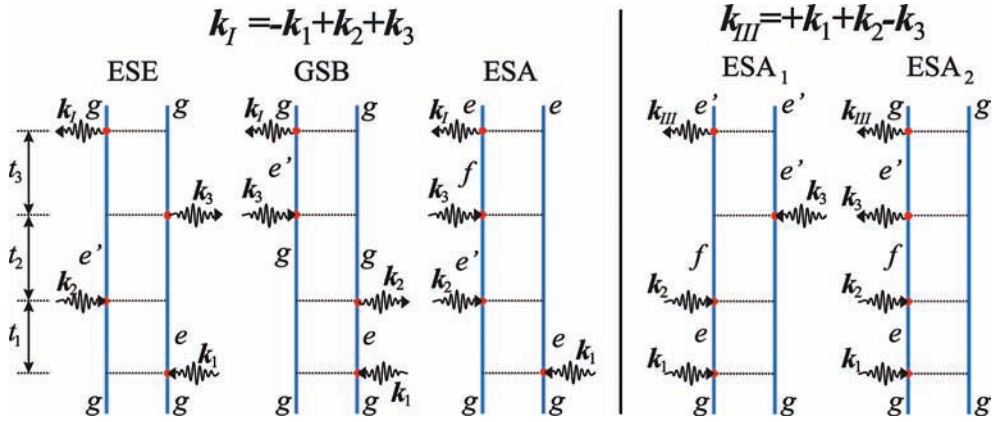

FIGURE 2. Feynman diagrams for two 2D signals with wavevectors $\mathbf{k}_I$ and $\mathbf{k}_{III}$. Incoming and outgoing arrows represent the interaction events; states of the system during various intervals between interactions are marked. ESA = excited-state absorption; GSB = ground-state bleaching; ESE = excited-state emission. For $S_{\mathbf{k}_I}$, the density matrix during (t_1, t_2, t_3) is (*ge*,*e*′*e*,*e*′*g*) for ESE, (*ge*,*gg*,*e*′*g*) for GSB, and (*ge*,*e*′*e*,*fe*) for ESA. For $S_{\mathbf{k}_{III}}$, both diagrams are of ESA type. The states of the density matrix are (*eg*,*fg*,*fe*′) for ESA_1 and (*eg*,*fg*,*e*′*g*) for ESA_2.

In the GSB pathway, the system returns to the ground state (described by the density matrix element ρ_{gg}), during the second interval t_2, after interacting with the first two pulses. The third interaction is affected by the decrease of the ground-state population, which reduces (bleaches) the subsequent photon absorption. In the ESE pathway, the system resides in the singly excited (*e*) manifold during t_2, and the third interaction brings it back to the ground state by stimulated emission. The ESA pathway shares the same t_1 and t_2 history of the ESE; however, the third interaction now creates a doubly excited state, *f*. The $S_{\mathbf{k}_I}$ signal is usually displayed as a frequency/frequency correlation plot $S_{\mathbf{k}_I}(\Omega_3, t_2, \Omega_1)$ obtained by a double Fourier transform with respect to the time delays t_1 and t_3, holding t_2 fixed. Ω_3 and Ω_1 reveal the various resonance transitions, as can be anticipated from the diagrams. Only single-exciton ω_{eg} resonances corresponding to optical coherences ρ_{eg} show up during t_1 and are projected onto the Ω_1 axis. The Ω_3 axis shows either $\omega_{e'g}$ resonances (ESE, GSB) or ω_{fe} (ESA). The t_2 evolution reflects exciton populations ρ_{ee} and intraband single-exciton coherences $\rho_{ee'}$. Population transport, coherence oscillations, and spectral diffusion dominate this interval in the ESE and ESA paths.[6]

Since the molecular frequencies during t_1 (ω_{ge}) are negative and during t_3 (ω_{eg} and ω_{fe}) are positive, the Ω_1 frequency axis is reversed in the 2D plots. With this convention, uncoupled excitons only show *diagonal* peaks. Off diagonal *cross-peaks* are markers of some kind of communication among various excitations, which causes their resonance frequency to be different during t_1 and t_3. This can be attributed either to exciton delocalization or to population transport. A simple interpretation of the signals is possible by using a basis of states localized on the various chromophores. Since the dipole is localized on each chromophore and can only excite one chromophore at a time, cross-peaks only appear when the chromophores are coupled. NMR spectra are similarly interpreted in terms of the couplings of localized spin states.[8] The couplings of chromophores can always be formally eliminated by diagonalizing the single-exciton Hamiltonian and switching to the delocalized exciton basis. However in this representation, the dipole operator matrix elements will depend on the details of the eigenstates, which prevents the simple intuitive interpretation of the signal.

The $S_{\mathbf{k}_{III}}$ technique has two ESA-type contributions (Figure 2). The 2D spectrum is obtained by correlating either $t_1 \rightarrow \Omega_1$ with $t_2 \rightarrow \Omega_2$, $S_{\mathbf{k}_{III}}(\Omega_1, \Omega_2, t_3)$, or $t_2 \rightarrow \Omega_2$ with $t_3 \rightarrow \Omega_3$, $S_{\mathbf{k}_{III}}(t_1, \Omega_2, \Omega_3)$. The density matrix evolution during t_1 and t_2 is identical for the ESA_1 and ESA_2 diagrams: single-exciton resonances corresponding to ρ_{eg} show up during t_1. During t_2, the system is in a coherent superposition (coherence), ρ_{fg}, between the doubly excited state *f* and the ground-state *g*. Two-exciton double-quantum-coherence resonances corresponding to the different doubly excited states *f* are then projected onto Ω_2. The t_3 evolution is very different: In ESA_1, the system is in a coherence between *f* and *e*′ ($\rho_{fe'}$), which results in resonances at $\Omega_3 = \omega_{fe'}$, corresponding to all possible transitions between doubly- and singly- excited states. For ESA_2, the system is in a coherence between *e*′ and *g* ($\rho_{e'g}$) and reveals single-exciton resonances at $\Omega_3 = \omega_{e'g}$ as t_3 is scanned. When the single-exciton states *e* and *e*′ do not interact (e.g., when they belong to two uncoupled chromophores), the corresponding two-exciton state is given by a direct product $|f\rangle = |ee'\rangle$ and the double-excitation energy is the sum $\varepsilon_f = \varepsilon_e + \varepsilon_{e'}$. In that case, $\omega_{eg} = \omega_{fe'} = \varepsilon_e$, the two diagrams exactly cancel, and the signal vanishes! The entire $S_{\mathbf{k}_{III}}$ signal is thus induced by correlations and its peak pattern provides a characteristic fingerprint for the correlated doubly excited wave functions. This conclusion

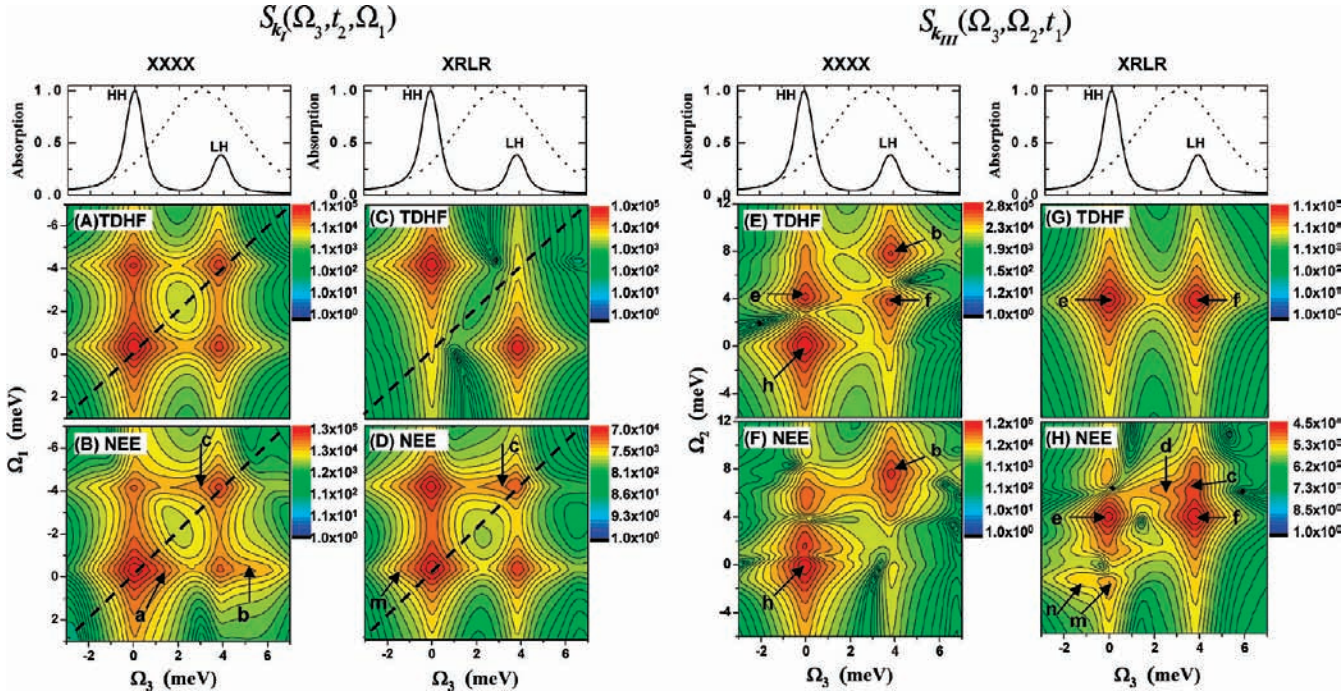

FIGURE 3. Simulated $S_{\mathbf{k}_I}(\Omega_3, t_2, \Omega_1)$ for $t_2 = 0$ fs (panels A−D) and $S_{\mathbf{k}_{III}}(\Omega_3, \Omega_2, t_1)$ for $t_1 = 0$ fs (panels E−H) spectra of a GaAs quantum well, calculated by a mean-field (TDHF) and a higher level (NEE) treatment of electron correlation using XXXX and XRLR pulse polarization configurations, as indicated. The frequency origin is set at the HH exciton energy ($e_H = 1520$ meV) along the Ω_3 and Ω_1 axes, and at twice the HH exciton energy ($2e_H$) along Ω_2. Top panels show the simulated linear absorption (—) and pulse power spectra (···) used for computing the 2D signals.

goes beyond the present simple model. $S_{\mathbf{k}_{III}}$ vanishes for uncorrelated many-electron systems described by the Hartree−Fock wave function and thus provides an excellent background-free probe for electron correlations.[12,20] The (Ω_2, Ω_3) correlation plots spread the two-exciton (*f* state) information along both axes, thus improving the resolution of the two-exciton manifold.

Signatures of Many-Electron Correlations in Semiconductor Quantum Wells

Semiconductor nanostructures can be fabricated with high purity allowing variation of parameters (e.g., confinement size, barrier height) one at a time. Such a degree of control is not possible in molecular aggregates. They therefore provide ideal systems for experimentally testing various levels of many-body theory and electronic structure calculations. One dimensional femtosecond four wave mixing spectroscopy has long been used for probing coherence and charge carrier dynamics in semiconductors.[21,30] Two dimensional extensions have recently been reported in quantum wells and quantum dots.[12−15]

Taking spin−orbit interaction and spatial confinement into account, excitons in GaAs quantum wells (QW) can be described using a single conduction band for electrons and two nondegenerate valence bands.[12] This results in heavy-hole (HH) and light-hole (LH) excitons. For a QW with 10 nm width, these give two absorption peaks at 0.0 and 3.8 meV (top panels of Figure 3; the origin is set at the 1520 meV HH exciton energy). There are three types of possible two-exciton states: pure HH/HH, pure LH/LH, and mixed LH/HH. The two-exciton states can be either bound (negative interaction energy) or unbound (positive, scattering energy), depending on the electron and hole spin configuration.

The following simulations used a three-band one-dimensional tight-binding Hamiltonian with periodic boundary conditions, which qualitatively reproduces the key features of the optical excitations of a QW of GaAs. The first two columns of Figure 3 show the simulated $S_{\mathbf{k}_I}(\Omega_3, t_2, \Omega_1)$ spectra for $t_2 = 0$ fs for two pulse polarization configurations XXXX (left column) and XRLR (next column). This notation gives the polarizations of the three excitation pulses and the final heterodyne pulse from right (first) to left (last): R, right-circularly polarized; L, left-circularly polarized; and X, linearly polarized along *x*. Two levels of theory were employed. The time-dependent Hartree−Fock (TDHF) includes an approximate mean-field treatment of electron correlations, while the nonlinear exciton equations (NEE) provide an exact treatment of correlations for the model Hamiltonian used.[6] We start with the XXXX

configuration. At the TDHF level (panel A), the two peaks along the diagonal dashed line represent HH ($e_H = 0$ meV) and LH ($e_L = 3.8$ meV) excitons. The cross-peaks indicate that the two types of excitons are coherently coupled. The NEE calculation shown in panel B reveals several additional features marked a, b, and c in the vicinity of the main peaks. The blue shoulder (b) represents mixed LH/HH two-excitons, the red shoulder (c) arises from bound LH/LH two-excitons, and the weak feature (a) is due to unbound HH/HH two-excitons. These are missed in the lower-level TDHF theory (panel A). Other polarization configurations and the $S_{k_{III}}$ technique are much more sensitive to electron correlations, as illustrated in the other panels. The second column represents the calculations for the XRLR polarization configuration. This eliminates the diagonal peaks in the TDHF (panel C). Consequently, in the NEE calculation (panel D), the features m and c arising, respectively, from bound HH/HH and LH/LH two excitons are better resolved, than in XXXX.

The corresponding $S_{\mathbf{k}_{III}}(\Omega_3, \Omega_2, t_1)$ signals for $t_1 = 0$ fs are shown in the right two columns. Panels E and F represent XXXX spectra. TDHF contributions h, b, e, and f from HH/HH, LH/LH, LH/HH, and HH/LH two excitons, respectively, are all present in panel E. These dominant TDHF contributions mask the weaker correlation effects in the NEE calculation (panel F). With XRLR polarization (panel G), only two peaks marked e and f are seen at the TDHF level.[13] These represent the contributions from mixed HH/LH two excitons. However, the TDHF contributions from either pure HH/HH two excitons at $(\Omega_3, \Omega_2) = (e_H, 2e_H) = (0, 0)$ meV or from pure LH/LH two excitons at $(\Omega_3, \Omega_2) = (e_L, 2e_L) = (3.8, 7.6)$ meV are eliminated. This makes it possible to probe weaker correlation effects beyond TDHF, as is demonstrated in the NEE simulation in panel H. In addition to the TDHF peaks e and f (same as those in panel G), we clearly see new features c, d, m, and n. Features m and n come from pure bound HH two excitons, and the correlation energy is given by the Ω_2 value of these peaks. Similarly, the Ω_2 shift of features c and d with respect to $e_L + e_H$ gives the correlation energy among pure bound LH two excitons.

These simulations demonstrate how TDHF and higher-order correlation effects may be separated by the $S_{\mathbf{k}_{III}}$ technique using the XRLR polarization configuration. This is not possible in the $S_{\mathbf{k}_i}$ signal due to the overlap between single-exciton (GSB and ESE) and two-exciton contributions (ESA). $S_{\mathbf{k}_i}$ and $S_{\mathbf{k}_{III}}$ provide complementary information. $S_{\mathbf{k}_{III}}$ offers a direct look at two-exciton correlations.[22] This experiment has been recently carried out in a GaAs quantum well.[23] The variation of $S_{\mathbf{k}_i}(\Omega_3, t_2, \Omega_1)$ with t_2, reveals exciton relaxation and transport. $S_{\mathbf{k}_{III}}$ is not sensitive to transport since exciton populations (ρ_{ee}) are never created.

Computing electron correlation effects, beyond the Hartree−Fock level, constitutes a major challenge of many-body theory. It is not possible to visualize the full correlated electronic wave functions, which live in a high-dimensional many-electron space. However, the various peaks of the $S_{\mathbf{k}_{III}}$ signal show the projections of the correlated two-exciton wave function onto various products of single-exciton states. This information is related to electron delocalization and coherences and goes beyond the charge density alone. The unique look into the many-body wave functions offered by 2D signals thus provides a direct experimental test for different approximate levels of theory for electron correlations.

Energy Transfer and Double-Quantum Coherence in Photosynthetic Complexes

The primary events driving the food chain are the absorption of sunlight by photosynthetic antennae and the subsequent transport of the excitations to reaction centers, where charge separation triggers a sequence of events that eventually convert the photon energy into chemical energy.[6] Multidimensional optical techniques can provide a unique probe for the entire energy and charge transfer pathway in a single measurement.[6,7,24,31] The Fenna−Matthews−Olson (FMO) complex from photosynthetic green sulfur bacteria made of seven bacteriochlorophyll *a* (BChl *a*) molecules (Figure 4a) mediates the energy transport between the primary antennae (the chlorosome) and the reaction center.

The 700 nm Q_y absorption band consisting of seven single-exciton states (Figure 4b) has four peaks. Two dimensional electronic spectra of this band have been measured.[7,24,31] The simulated 2D $S_{\mathbf{k}_i}(\Omega_3, t_2, \Omega_1)$ XXXX signal is depicted in Figure 4c. Diagonal peaks show the main exciton resonances, whereas the cross-peaks reveal the couplings between the BChl chromophores, and their intensities provide direct signatures of structure (distances between chromophores). The line shape dynamics of diagonal peaks and the ratio of linewidths along and across the diagonal are direct measures of frequency fluctuation correlation functions. The peak elongation along the diagonal line is a signature of static (inhomogeneous) broadening, indicating that the resonance frequency is the same during t_1 and t_3.

The energy-transfer pathways can be monitored through the variation of the various peak intensities with the delay t_2. At $t_2 = 0$, the blue region of the signal, which represents GSB and ESE, is elongated along the diagonal line. The green regions originate from the double-exciton states associated

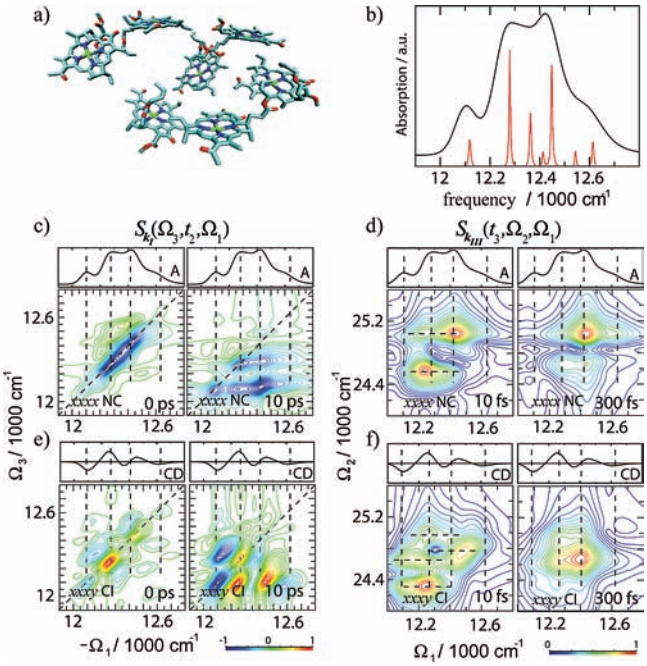

FIGURE 4. Two dimensional signals of the Q_y band of the FMO complex from *Chlorobium tepidum*. (a) arrangement of BChls in the FMO complex; (b) absorption (oscillator strength of each exciton is represented by the red line); (c, e) the 2D $S_{\mathbf{k}_I}(\Omega_1, t_2, \Omega_3)$ using XXXX (imaginary part) and XXXY (real part) pulse polarizations. The t_2 delay time is indicated on each panel. (d, f) Absolute value of the 2D $S_{\mathbf{k}_{III}}(\Omega_1, \Omega_2, t_3)$ signal using XXXX and XXXY pulse polarizations. The t_3 delay time is indicated on each panel.

with the ESA. The absorption spectrum is displayed on top of the 2D graphs. At $t_2 = 10$ ps, we see major changes in the peak pattern, due to exciton transport among the excited states. The blue regions around $\Omega_3 = 12\,000$ and $12\,200$ cm^{-1} show emission from the two lowest exciton states after energy relaxation.

Chirality-induced (CI) signals can probe exciton structure, fluctuations, and dynamics with a remarkable sensitivity. CI signals are obtained by specific pulse polarization configurations which change sign when the sense of chirality is reversed. By design, such signals vanish for nonchiral systems or in racemic mixtures. They are given by the first-order in wavevector corrections to the nonchiral (NC) zeroth order response in the dipole approximation and are $\sim 10^{-2}$ weaker.

The simulated $S_{\mathbf{k}_I}$ CI XXXY signal (Figure 4e) shows a very different pattern than the NC XXXX. At $t_2 = 0$, various peaks are distributed along the diagonal and have alternating signs. The streaks of single-color peaks at constant Ω_3 follow the peaks of the circular dichroism (CD) spectrum shown at the top margin. They reveal single-exciton resonances with higher resolution. Five single-exciton peaks may be identified (compared with four in XXXX). The CI signal shows that the third $12\,400$ cm^{-1} absorption peak is made of several overlapping contributions. These generate a doublet with opposite signs in CD and 2D CI signal. At 10 ps delay, the peaks move to the off-diagonal region of smaller Ω_3 due to population transport. The peaks for a fixed Ω_3 alternate signs, as in CD. The resolution is highly improved by the sign alternation.

The d panels in Figure 4 display the absolute magnitude of $S_{\mathbf{k}_{III}}(t_3, \Omega_2, \Omega_1)$ (XXXX) signal for two delay times t_3, as indicated. Double-exciton resonances are seen along Ω_2. The FMO complex has 21 double-exciton states; however, only two dominate the signal. Peak positions along Ω_1 represent the projections of the double-exciton wave function into various products of single excitons.[6] Two single excitons are seen at $t_3 = 10$ fs (compare with the absorption given on the top margin). The dominant double excitons are localized primarily on this pair of single-exciton states. Variation with t_3 reveals the evolution of double-exciton states projected into the space of single-exciton products. At 300 fs, one two-exciton state given by a doubly excited single-exciton mode dominates the signal. The corresponding CI XXXY signal shown in the bottom row (f) reveals a richer double-exciton pattern; four double-exciton states are now clearly resolved. As in the CI $S_{\mathbf{k}_I}$, panel e, the Ω_1 axis resembles the CD spectrum. We note that the strongest double excitons are those associated with the most chiral distribution of pigments. At 300 fs, we observe dramatic localization of peaks in the double-exciton and single-exciton space. This dynamics is caused by coherent double-exciton evolution and its interference with single excitons.

Specific superpositions of $S_{\mathbf{k}_I}$ signals with various polarization configurations can separate the population transport pathways from coherence oscillations. In Figure 5, we demonstrate how such NC configurations may be used to distinguish between two species of FMO-containing bacteria: *Chlorobium tepidum* (*C.t.*, left panels) and *Prosthecochloris aestuarii* (*P.a.*,[25] right panels). The FMO complexes of both species have essentially an identical pigment configuration. Spectral differences are caused by the different protein environments. In the top row, we show snapshots of XXXX signals (as in Figure 4). In the lower three rows, we present three combinations of polarization configurations designed to enhance specific features.[6,25] Signal A (second row) highlights the exciton coherent and incoherent dynamics during t_2 by eliminating static background: it vanishes at 0 delay, then builds up in 100 fs and shows large changes up to 5 ps. This dynamics is further elucidated by the other two signals, B and C. The B signal (third row) reveals rapid few hundred femtosecond decay of exciton coherences by eliminating all population-including contributions to the signal during t_2. At short delays (0−50 fs), it reveals various peaks distributed in antidiagonal pat-

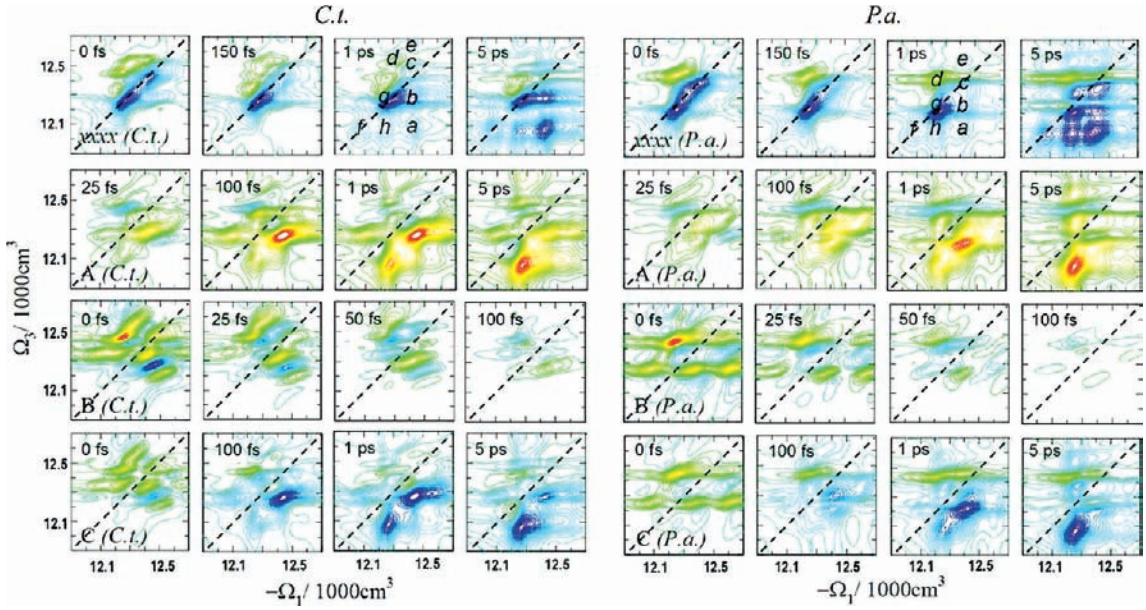

FIGURE 5. 2D $S_{\mathbf{k}_i}(\Omega_1, t_2, \Omega_3)$ signals of the Q_y band of the FMO complexes from two species of bacteria: *Chlorobium tepidum* (*C.t.*) and *Prosthecochloris aestuarii* (*P.a.*). A, B, and C signals are given by the following superpositions of pulse polarizations: $A = S^{(3)}_{xxyy}(\Omega_3, t_2, \Omega_1) - S^{(3)}_{xyxy}(\Omega_3, t_2, \Omega_1)$; $B = S^{(3)}_{xyxy}(\Omega_3, t_2, \Omega_1) - S^{(3)}_{xyyx}(\Omega_3, t_2, \Omega_1)$; $C = S^{(3)}_{xxyy}(\Omega_3, t_2, \Omega_1) - S^{(3)}_{xyyx}(\Omega_3, t_2, \Omega_1)$.

tern around 12 300 cm^{-1}. Between 0 and 50 fs, the peak pattern does not change, indicating that the quantum evolutions of density matrix coherences are decoupled within the secular approximation used in our simulations.

The C signal (fourth row) highlights exciton hopping during t_2. Strong diagonal peaks are eliminated and the exciton states participating in primary energy transport in the off-diagonal regions at 100 fs are clearly seen. Between 150 fs and 5 ps, the initial cross-peak configuration changes to reflect the thermal equilibrium of excitons. The exciton states can be identified from peak positions, and thus the energy transport pathways can be deduced. The strongest cross-peak indicates that early transport in the region 12 500−12 570 cm^{-1} involves excitons 3, 4, and 5 (exciton states are numbered in increasing-energy order). A different peak becomes dominant at long (5 ps) delay indicating energy trapping in the lowest state 1. Intermediate steps can be followed through other off-diagonal peaks. B-type signals for the *C.t.* and *P.a.* species are very different, whereas the C signals are similar. This indicates that energy transport pathways in the two species are similar, even though the exciton coherences and exciton delocalization patterns are different.[25]

Attosecond snapshots of valence electronic excitations: Resonant X-ray Spectroscopy of Core Excitons

X-ray pulses offer much higher spatial and temporal resolution than possible in the visible regime. Two dimensional X-ray correlation spectroscopy (2DXCS) can provide an attosecond, atomic-scale window into the valence electronic structure and chemical dynamics.

Impulsive 100 fs lasers, shorter than typical molecular vibrational periods, made it possible in the 1980s to excite vibrations coherently and observe vibrational wavepackets in real time.[26] Attosecond X-ray pulses are shorter than inverse valence electron transition frequencies and can similarly excite wavepackets of valence electrons impulsively, as permitted by their broad bandwidth, making it possible to observe motions of electrons in real space and time.

When an X-ray photon is absorbed, a core−shell electron is excited into bound unoccupied or continuum states. Because the core−shell is highly localized, resonances in X-ray absorption spectroscopy (XAS) near the ionization edge provide information about the valence unoccupied states in the vicinity of the nucleus. The core hole is filled within a few femtoseconds either radiatively (X-ray fluorescence) or by an Auger process. The process is accompanied by valence electron excitations. Resonances in the resulting X-ray inelastic scattering (RIXS) and emission (XES) spectra provide information about occupied valence electronic states. Because binding energies of 1s electrons in first-row atoms differ by 60−150 eV, one can selectively probe different regions in a molecule by tuning the incident soft X-ray photon frequency to a particular atom. XAS and XES thus provide atom-specific probes of valence electronic structure of molecules.

In contrast to (off-resonant) X-ray diffraction, the spatial resolution in the resonant spectroscopy considered here is not directly related to the short wavelength but rather to the highly localized nature of the core orbitals. We next turn to the temporal resolution. Time-resolved XAS employs femtosecond X-ray pulses to resolve nuclear dynamics and observe transition species in photochemical reactions.[16] Attosecond X-ray pulses have been produced by high-harmonic generation (HHG).[17,19] Fourth-generation synchrotron sources based on the X-ray free-electron laser (XFEL) can provide 100 fs X-ray pulses of brilliance that exceeds existing X-ray sources by many orders of magnitude. Future developments in technology that will combine the pulse coherence of HHG with the brilliance of XFEL may ultimately result in multiple X-ray pulses with the controlled timing, phase, and intensity necessary to perform phase-coherent attosecond all-X-ray four-wave mixing measurements.

$S_{\mathbf{k}_I}$ signals in a molecule where pulses 1 and 2 are tuned to one core transition (say N K-edge) and pulses 3 and 4 are resonant with a different transition (say O K-edge)[27] can show the interference between ESE and GSB quantum pathways that involve only singly core-excited states, and ESA pathways that involve singly and doubly core-excited states. If the frequency of a given core−shell transition is independent of whether another core−shell is excited, the ESA contribution interferes destructively with the ESE and GSB and the cross-peaks vanish. The coupling between two transitions results in a distinct 2DXCS cross-peak pattern. This is in striking contrast to XAS and XES, which are *additive,* that is, the contribution of two independent transitions is the sum of the individual transitions. 2DXCS provides a direct probe into the electronic and molecular structure through the coupling between core transitions that depends on the distance between the core shells, as well as their electronic environment, while retaining the element specificity of XAS and XES.

The left column of Figure 6 depicts the simulated N1s and O1s XAS and $S_{\mathbf{k}_I}$ N1s/O1s 2DXCS signal of the para and ortho isomers of aminophenol.[27] The first two pulses are tuned to the N K-edge (401 eV) and the other two are near the O K-edge (537 eV). We assume rectangular pulse envelopes $E_j(\omega)$ with a 6 eV bandwidth centered around the carrier frequencies. The molecular eigenstates were described by singly and doubly substituted Kohn−Sham (KS) determinants in the equivalent-core approximation.[27] The calculated N 1s XAS of *para-* and *ortho*-aminophenol closely resemble the experimental inner-shell electron energy loss spectra (ISEELS) of aniline shown in Figure 6a, indicating that the amine XAS only weakly depends on whether the hydroxyl group is in the para

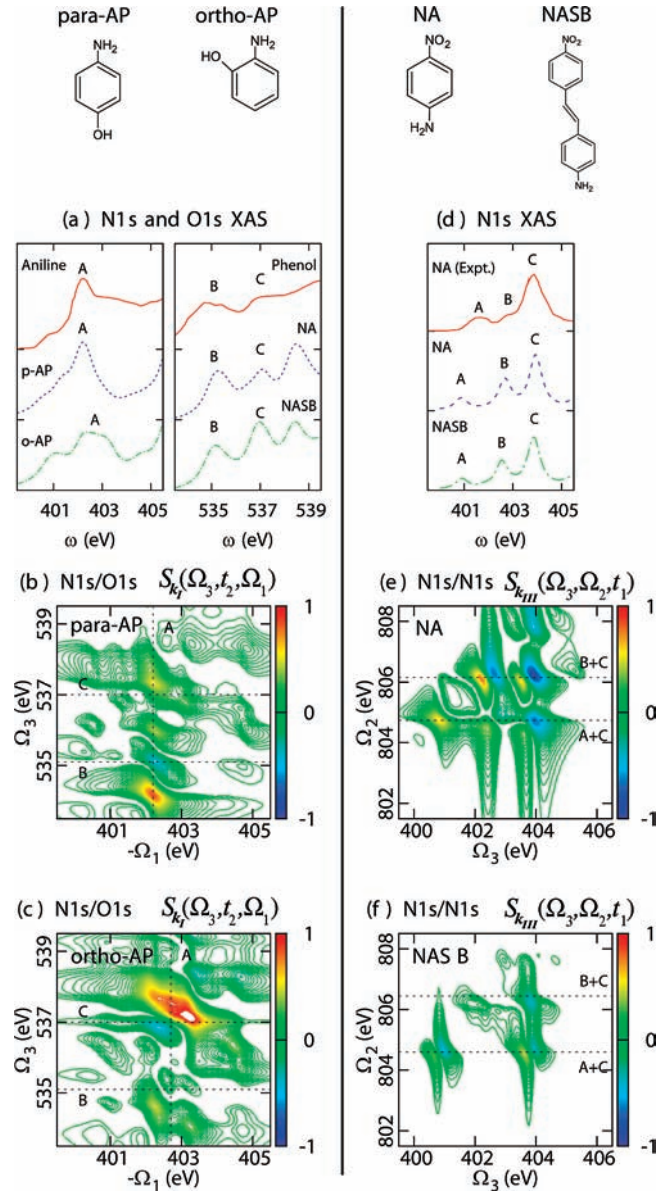

FIGURE 6. Left panel: (a) N 1s and O 1s XAS of *para*-aminophenol (*p*-AP, blue) and *ortho*-aminophenol (*o*-AP, green) compared with experimental ISEELS of aniline and phenol (red); (b) N 1s/O 1s $S_{\mathbf{k}_I}(\Omega_3, t_2{=}0, \Omega_1)$ 2DXCS of *para*-aminophenol; (c) N 1s/O 1s $S_{\mathbf{k}_I}(\Omega_3, t_2{=}0, \Omega_1)$ 2DXCS of *ortho*-aminophenol. Right panel: (d) N 1s XAS of *para*-nitroaniline (NA, blue) and 4-nitro-4′-aminestilbene (NASB, green) compared with experimental ISEELS of *para*-nitroaniline (red); (e) $S_{\mathbf{k}_{III}}(\Omega_3, \Omega_2, t_1)$ 2DXCS of *para*-nitroaniline; (f) $S_{\mathbf{k}_{III}}(\Omega_3, \Omega_2, t_1)$ 2DXCS of 4-nitro-4′-aminestilbene.

or ortho position or is not present at all. Similarly, the O 1s XAS is virtually independent of the position of the amine group and similar to the ISEELS of phenol. The situation is markedly different for the N/O 2DXCS cross-peaks, because the effect of the N 1s transitions on the O 1s absorption strongly depends on the relative position of two atoms. The $S_{\mathbf{k}_I}$ of the *para*-aminophenol (Figure 6b) is weaker than that of the ortho isomer (Figure 6c) since the amine and hydroxy

groups are further apart and their coupling is weaker. Furthermore, the cross-peaks provide information about the core excited-state wave functions beyond the dipole coupling available in XAS. In particular, a strong contribution to XAS but weak 2DXCS cross-peak indicates localization of the promoted core electron to the atom in resonance. The reverse pattern will indicate the delocalization of the promoted core electron over the two atoms whose core shells are in resonance.

Note that the $S_{\mathbf{k}_i}$ signals shown in Figure 6 only cover the cross-peak region that is accessible by our pulses (first two resonant with the N, the other two with O). However, transitions involving two different or the same core−shells may contribute to the signal provided the chemical shifts (a few electronvolts) are smaller than the pulse bandwidths and the 2DXCS diagonal and cross-peaks spectrally overlap. Due to interference, the latter are usually weaker, and a higher spectral resolution is required in order to separate the cross-peaks and extract the couplings.

$S_{\mathbf{k}_{III}}$ signals only contain features induced by the coupling between core transitions. The simulated N 1s XAS and $S_{\mathbf{k}_{III}}$ 2DXCS signals of benzene and stilbene disubstituted with the amine and nitroso groups are shown in Figure 6 (right panel).[18] The calculated XAS of *para*-nitroaniline (NA) and 4-nitro-4′-aminestilbene (NASB) are qualitatively similar to the experimental ISEELS spectra of nitroaniline (Figure 6d). This is in accordance with the building-block principle of XANES spectroscopy, which states that the contributions of multiple core shells (in this case, amine and nitroso) are additive. The N 1s $S_{\mathbf{k}_{III}}$ of NA and NASB obtained with four 402.6 eV pulses are shown, respectively, in Figure 6e,f. There are three core-excited states with significant dipole strength in the XAS of NA: two correspond to excitation of the amine core electron (states A and B) and one to the excitation of the nitroso core electron (state C). Despite the much weaker dipole strength of transition A, the strong coupling between the A and C transitions results in an intense 2DXCS feature. Comparison of the equivalent-core orbitals describing the promoted core electron in the singly and doubly excited states[18] shows that in state A the promoted core electron is delocalized; hence, states A and C are strongly coupled. State B, in contrast, is localized at the amine group; hence, the coupling between states B and C is weaker, and the 2DXCS signal is weak due to negative interference between the ESA_1 and ESA_2 contributions.

Similar to NA, there are three core-excited states with a significant dipole strength in the XAS of NASB: two due to excitation of the amine core electron (states A and B) and one due to the excitation of the nitroso core electron (state C). Given the similarity of the XAS spectra, the ESA_1 and ESA_2 contributions to NASB signal are similar to NA, with the strongest feature corresponding to the double-excitation corresponding to states B and C.[18] However, overall, the $S_{\mathbf{k}_{III}}$ signal is much weaker than that of NA, indicating that these states are uncoupled in the doubly excited states. Examination of the ECA orbitals[18] shows that indeed the B state is strongly localized on the amine group. In NASB, the amine and nitroso groups are separated by 12.3 Å compared with 5.6 Å in NA; hence, the coupling between the B state (localized on amine group) and the C state (localized on the nitroso group) is much weaker than the coupling between these states in NA. State A is delocalized, and its coupling with state C is significant resulting in the characteristic two cross-peak pattern. $S_{\mathbf{k}_{III}}$ is thus highly sensitive to the separation between the core−shell as well as the localization of the corresponding core-excited states.

2DXCS could provide a novel window for studying strongly correlated materials, extending the information gained by standart inelastic X-ray scattering.[28]

This research was supported by the National Institutes of Health (Grant GM59230), National Science Foundation (Grant CHE-0745892), and the Chemical Sciences, Geosciences and Biosciences Division, Office of Basic Energy Sciences, Office of Science, U.S. Department of Energy.

BIOGRAPHICAL INFORMATION

Shaul Mukamel, currently the Chancellor Professor of Chemistry at the University of California, Irvine, received his Ph.D. in 1976 from Tel Aviv University and has held faculty positions at Rice University, the Weizmann Institute, and the University of Rochester. He is the recipient of the Sloan, Dreyfus, Guggenheim, the Alexander von Humboldt Senior Scientist awards, and the Lippincort Award and is a fellow of the American Physical Society and the Optical Society of America. His interests focus on the theory of ultrafast nonlinear spectroscopy of molecules and semiconductor nanostructures, attosecond X-ray spectroscopy, many-body effects in quantum optics, and nonequilibrium fluctuations in open systems. He is the author of the textbook *Principles of Nonlinear Optical Spectroscopy*.

Darius Abramavicius was born in 1974 in Alytus, Lithuania. He received his Ph.D. degree under the supervision of Prof. Leonas Valkunas from the Institute of Physics and Vytautas Magnus University in 2002 in Lithuania. He later worked in the group of Prof. S. Mukamel at University of Rochester and University of California, Irvine. During 2005−2006, he had a lecturer position in Vilnius University (Lithuania). Currently he is an assistant specialist at the University of California, Irvine. His research interests are in the field of optical properties of molecular complexes.

Lijun Yang was born in 1968 in Pingyao, China. He received his Ph.D. in physics from Queen's University at Kingston, Canada, in

2005 under the supervision of Prof. Marc M. Dignam. Since then, he has been working as a postdoctoral researcher in Prof. Mukamel's group in the chemistry department of University of California, Irvine. His research interests include the theoretical and computational studies on the ultrafast dynamics of semiconductor nanostructure and molecular complexes. He had taught as a lecturer for four years in Harbin Institute of Technology in China and worked with Prof. Wanzhen Geng on infrared imaging techniques applied to nondestructive testing.

Wei Zhuang received his Ph.D. in chemistry from University of California, Irvine, in 2007 under the supervision of Prof. Shaul Mukamel. Since then, he has been working as a postdoctoral researcher in Prof. D. Chandler's research group in the chemistry department of University of Califoria, Berkeley. His research interests include molecular dynamics of water, polypeptides, and proteins.

Igor V. Schweigert was born in Novosibirsk, Russia, in 1978. He received his Ph.D. in Chemistry from the University of Florida, Gainesville, in 2005. He then joined Prof. S. Mukamel's group as a Postdoctoral Associate. In 2007, he received a postdoctoral fellowship from the National Research Council of the National Academies and joined the Theoretical Chemistry Section at the U.S. Naval Research Laboratory. His research interests include theoretical modeling of electronic spectra, ab initio molecular dynamics of chemical reactions, and developing novel electronic structure methods that combine the density functional and wave function based approaches.

Dmitri V. Voronine was born in 1979 in Moscow, Russia, and is currently a postdoctoral researcher in the group of Prof. T. Brixner at the Universität Würzburg, Germany. He received his Ph.D. in 2004 from the Center for Photochemical Sciences, Bowling Green State University, with Prof. M. A. J. Rodgers and later worked with Prof. S. Mukamel at the University of California, Irvine. He has been the recipient of the McMaster Fellowship (BGSU) and the RCCM Excellent Young Investigator award (Würzburg). His research interests include coherent control with laser pulse shaping in femtosecond multidimensional spectroscopy and ultrafast nanooptics.

FOOTNOTES

*E-mail: smukamel@uci.edu.

‡Present address: Deparment of Chemistry, University of California, Berkeley, CA.

¶Present address: Theoretical Chemistry Section, US Naval Research Laboratory, Washington, DC.

§Present address: Institut für Physikalische Chemie, Universität Würzburg, Germany.

REFERENCES

1 Tanimura, Y.; Mukamel, S. Two-dimensional femtosecond vibrational spectroscopy of liquids. *J. Chem. Phys.* **1993**, *99*, 9496–9511.

2 Mukamel, S. Multidimensional femtosecond correlation spectroscopies of electronic and vibrational excitations. *Annu. Rev. Phys. Chem.* **2000**, *51*, 691–729.

3 Hochstrasser, R., Ed. Multidimensional ultrafast spectroscopy special feature. *Proc. Natl. Acad. Sci. U.S.A.* **2007**, *104*, 14189−14242.

4 Jonas, D. M. Two-dimensional femtosecond spectroscopy. *Annu. Rev. Phys. Chem.* **2003**, *54*, 425–463.

5 Zhuang, W.; Hayashi, T.; Mukamel, S. Coherent multidimensional vibrational spectroscopy of biomolecules; concepts, simulations and challenges *Angew. Chem.*, in press.

6 Abramavicius, D.; Palmieri, B.; Voronine, D. V.; Šanda, F.; Mukamel, S. Coherent multidimensional optical spectroscopy of excitons in molecular aggregates; quasiparticle vs. supermolecule perspectives. *Chem. Rev.*, in press.

7 Cho, M. Coherent two-dimensional optical spectroscopy. *Chem. Rev.* **2008**, *108*, 1331–1418.

8 Ernst, R. R.; Bodenhausen, G.; Wokaun, A. *Principles of Nuclear Magnetic Resonance in One and Two Dimensions*; Clarendon Press: Oxford, U.K., 1998.

9 Wüthrich, K. NMR studies of structure and function of biological macromolecules (Nobel Lecture). *Angew. Chem., Int. Ed.* **2003**, *42*, 3340–3363.

10 Chernyak, V.; Zhang, W. M.; Mukamel, S. Multidimensional femtosecond spectroscopies of molecular aggregates and semiconductor nanostructures: The nonlinear exciton equations. *J. Chem. Phys.* **1998**, *109*, 9587–9601.

11 *Ultrafast Phenomena XVI*; Corkum, P., De Silvestri, S., Nelson, K., Riedle, E., Schoenlein, R., Eds.; Springer: 2009, ISBN: 978-3-540-95945-8 (in press).

12 Mukamel, S.; Oszwaldowski, R.; Yang, L. A coherent nonlinear optical signal induced by electron correlations. *J. Chem. Phys.* **2007**, *127*, 221105.

13 Yang, L.; Mukamel, S. Revealing exciton-exciton couplings in semiconductors using multidimensional four-wave mixing signals. *Phys. Rev. B* **2008**, *77*, 075335.

14 Erementchouk, M.; Leuenberger, M. N.; Sham, L. J. Many-body interaction in semiconductors probed with two-dimensional Fourier spectroscopy. *Phys. Rev. B* **2007**, *76*, 115307.

15 Li, X.; Zhang, T.; Borca, C. N.; Cundiff, S. T. Many-body interactions in semiconductors probed by optical two-dimensional fourier transform spectroscopy. *Phys. Rev. Lett.* **2006**, *96*, 057406.

16 Pfeifer, T.; Spielmann, C.; Gerber, G. Femtosecond X-ray science. *Rep. Prog. Phys.* **2006**, *69*, 443–505.

17 Corkum, P. B.; Krausz, F. Attosecond science. *Nat. Phys.* **2007**, *3*, 381–387.

18 Schweigert, I. V.; Mukamel, S. Double-quantum-coherence attosecond X-ray spectroscopy of spatially-separated, spectrally-overlaping core-electron transitions. *Phys. Rev. A* **2008**, *78*, 052509.

19 Kapteyn, H.; Cohen, O.; Christov, I.; Murnane, M. Harnessing attosecond science in the quest for coherent X-rays. *Science* **2007**, *317*, 775–778.

20 Li, Z.; Abramavicius, D.; Mukamel, S. Probing electron correlations in molecules by two-dimensional coherent optical spectroscopy. *J. Am. Chem. Soc.* **2008**, *130*, 3509–3515.

21 Rossi, F.; Kuhn, T. Theory of ultrafast phenomena in photoexcited semiconductors. *Rev. Mod. Phys.* **2002**, *74*, 895–950.

22 Yang, L.; Mukamel, S. Two-dimensional correlation spectroscopy of two-exciton resonances in semiconductor quantum wells. *Phys. Rev. Lett.* **2008**, *100*, 057402.

23 Stone, K. W.; Gundogdu, K.; Turner, D. B.; Li, X.; Cundiff, S. T.; Nelson, K. A. Two-quantum 2D FT electronic spectroscopy of biexcitons in GaAs quantum wells. *Science*, **2009**, in press.

24 Engel, G. S.; Calhoun, T. R.; Read, E. L.; Ahn, T. K.; Mančal, T.; Cheng, Y. C.; Blankenship, R. E.; Fleming, G. R. Evidence for wavelike energy transfer through quantum coherence in photosynthetic systems. *Nature* **2007**, *446*, 782–786.

25 Voronine, D. V.; Abramavicius, D.; Mukamel, S. Chirality-based signatures of local protein environments of photosynthetic complexes of green sulfur bacteria. Simulation study. *Biophys. J.* **2008**, *95*, 4896–4907.

26 Rosker, M. J.; Dantus, M.; Zewail, A. H. Femtosecond clocking of the chemical bond. *Science* **1988**, *241*, 1200–1202.

27 Schweigert, I. V.; Mukamel, S. Probing interactions between core-electron transitions by ultrafast two-dimensional X-ray coherent correlation spectroscopy. *J. Chem. Phys.* **2008**, *182*, 184307.

28 Devereaux, T. P.; Hackl, R. Inelastic light scattering from correlated electrons. *Rev. Mod. Phys.* **2007**, *79*, 175–233.

29 Mukamel, S. Principles of nonlinear optical spectroscopy (Oxford University Press, New York, 1995).

30 Chemla, D. S.; Shah, J. Many-body and correlation effects in semiconductors. *Nature* **2001**, *411*, 549–557.

31 Brixner, T.; Stenger, J.; Vaswani, H. M.; Cho, M.; Blankenship, R. E.; Fleming, G. R. Two-dimensional spectroscopy of electronic couplings in photosynthesis. *Nature* **2005**, *434*, 625–628.